



A semi-automatic procedure to support the detection of rapid-moving landslides using spaceborne SAR imagery

Giuseppe Esposito¹, Ivan Marchesini², Alessandro Cesare Mondini², Paola Reichenbach², Mauro Rossi², Simone Sterlacchini³

- 5 ¹National Research Council, Research Institute for Geo-Hydrological Protection (CNR-IRPI), Rende (CS), 87036, Italy
²National Research Council, Research Institute for Geo-Hydrological Protection (CNR-IRPI), Perugia, 06128, Italy
³National Research Council, Research Institute for the Dynamics of Environmental Processes (CNR-IDPA), Milano, 20126, Italy

Correspondence to: Giuseppe Esposito (giuseppe.esposito@irpi.cnr.it)

10 **Abstract.** The increasing availability of free-access satellite data represents a relevant opportunity for the analysis and assessment of natural hazards. The systematic acquisition of spaceborne imagery allows monitoring areas prone to geo-hydrological disasters, providing relevant information for risk evaluation and management. In case of major landslide events, for example, spaceborne radar data can provide an innovative solution for the detection of slope failures, even in case of persistent cloud cover. The information about extension and location of the landslide-affected areas may support decision-making processes during the emergency responses.

15 In this paper, we present a semi-automatic procedure, based on Sentinel-1 Synthetic Aperture Radar (SAR) images, aimed to facilitate the detection of rapid-moving landslides. The procedure evaluates changes of radar backscattered signals associated to land cover modifications, that may be also caused by mass movements. The procedure requires an initial manual selection of some parameters, and is able to execute automatically the download and pre-processing of images, the detection of SAR amplitude changes, and the identification of areas potentially affected by landslides, which are then displayed in a geo-referenced map. This map should help decision-makers and emergency managers to organize field investigations. The processes automatization is implemented with specific scripts running on a GNU/Linux operating system and exploiting modules of Open Source software.

20 We tested the processing chain, in back analysis, on an area of about 3000 km² in central Papua New Guinea that in February/March 2018 was struck by a severe seismic sequence that triggered numerous widespread landslides. In the area, we simulated a periodic survey of about seven months, from 12 November 2017 to 6 June 2018, downloading 36 Sentinel-1 images and performing 17 change detection analyses automatically. The procedure resulted in statistical and graphical evidences of widespread land cover changes occurred just after the most severe seismic events. Most of them can be interpreted as mass movements triggered by the main seismic shocks.

30



1 Introduction

Landslide recognition and mapping in rural areas represents one of the main challenges faced by the research community. The spatial and temporal distribution of landslides is well known mainly in urban areas, where they often cause severe consequences to anthropic structures and population. On the contrary, landslides in rural and remote areas remain often unknown, limiting environmental evaluations like hazard and risk assessment (Guzzetti et al., 2012). Understanding where landslides have occurred may provide useful indications to forecast future events. In particular, the knowledge of the spatial distribution of landslides in a given region is essential to implement, calibrate and validate statistically and physically based methods (Rossi and Reichenbach, 2016; Mergili et al., 2014a; Mergili et al., 2014b) aimed to predict the possible location of future mass movements or to identify areas where the probability of failure is negligible (Marchesini et al., 2014). As stated by Reichenbach et al. (2018), the quality and completeness of the landslide inventories may affect the reliability of the landslide susceptibility assessment (Steger et al., 2016). To produce inventory maps with limited errors and uncertainties (Santangelo et al., 2015), the mapping techniques should be selected taking into account a series of factors: the purpose of the inventory, the extent of the study area (Bornaetxea et al., 2018), the scale of the base maps, resolution and characteristics of the available data, the skills and experience of the investigators, and the available resources (Guzzetti et al., 2000; van Westen et al., 2006, Casagli et al., 2017).

Besides conventional techniques (field mapping, visual interpretation of aerial photographs), remote sensing technologies based on satellite optical imagery, airborne/terrestrial laser scanning and digital photogrammetry represent innovative solutions for landslide detection and mapping. Recently, also multispectral and Synthetic Aperture Radar (SAR) satellite images have been used with great success. To recognize landslides in multispectral and Very High Resolution (VHR) optical images, the most applied methods consist in the visual interpretation (Fiorucci et al., 2011; Ma et al., 2016) or in the semi-automatic classification (segmentation) that exploits different radiometric signatures of stable and failed areas (Martha et al., 2011; Mondini et al., 2011, Alvioli et al., 2018). However, optical images have some disadvantages and cannot be used when the analyzed areas are covered by persistent clouds or affected by shadow effects. To overcome these issues, SAR data can represent an effective alternative, since they are not influenced by weather conditions.

Several techniques allow extracting information from SAR data to identify and map slope failures. The Differential Interferometric Synthetic Aperture Radar (DInSAR) (Gabriel et al., 1989) has been widely used to detect surface displacements over large areas with sub-centimeter accuracy. DInSAR is aimed to calculate phase differences between two or more multi-temporal images and has been successfully applied to analyze landslides (Calò et al., 2012; Zhao et al., 2012; Cigna et al., 2013; Calvello et al., 2017; Tessari et al., 2017), earthquakes, subsidence, soil consolidation, volcanoes and tectonic deformations (Plank, 2014 and references therein). Other techniques exploit the amplitude information contained in the pixels of the SAR images. Amplitude of the backscattered signal is influenced by the type of target and varies according to several factors, such as the type of land use (e.g., water bodies, ice cover, forest type, bare soil), the surface roughness and the terrain slope. According to Colesanti and Wasowski (2006), amplitude SAR imagery represents potentially a very useful



65 source of information, which can complement high resolution optical imagery and aerial photography in feature detection. Generally, amplitude-based methods analyze the correlation of the speckle pattern of two images (e.g., pre- and post-event, where the terms “event” can refer to a major natural and/or human-induced hazard affecting a given area, as an earthquake, an hurricane, a forest fire, etc.) to map the land cover changes (Raspini et al., 2017). To date, the landslide mapping community has shown a poor attitude in using this type of product, so that only few studies have demonstrated the valuable contribution of SAR amplitude changes in landslide detection and mapping. According to Mondini (2017), this is due to a series of problems and drawbacks represented by: 1) the complex pre-processing procedures; 2) the acquisition geometry that can affect the quality of the images over mountainous areas where landslides are likely to occur; 3) the difficulty in using the SAR signal in traditional statistical classification approaches mainly due to speckling. A successful example of the use of amplitude variations of the radar signal to analyze landslides is described by Zhao et al. (2013), which inferred the Jiweishan rock slide in China using changes in SAR backscattering intensity in ALOS/PALSAR images. Tessari et al. (2017) verified that when the phase information cannot be exploited, amplitude of the reflected signal is very useful to detect and map rapid-moving landslides that cause significant variations in the ground morphology and land cover. Mondini (2017) proved that both landslides and flooded areas can be detected by verifying changes in the spatial autocorrelation in a multi-temporal series of SAR images. Konishi and Suga (2018) also identified a series of landslides in Japan by analyzing intensity correlation between pre- and post-event SAR images.

Besides the described techniques, recent advances in SAR technology are promoting the use of polarimetric SAR data (PolSAR) characterized by full-polarimetric information (i.e., acquired in single polarization, dual polarization, and fully polarimetric modes) for a target in the form of the scattering matrix (Skriver, 2012). According to Plank et al. (2016), these data provide more information on the ground, which enables a better land cover classification and landslide mapping. Successful applications were described by Yamaguchi (2012), Shimada et al. (2014), Li et al. (2014) and Plank et al. (2016). The use of SAR data to analyze landslides and/or potentially unstable slopes should hence increase, also in relation to a series of valuable technical innovations. The improved revisiting times and spatial resolution of the images, for example, represent a key factor during disaster response operations, when a preliminary localization of areas potentially affected by major landslides is crucial. Revisiting times have been in fact reduced from 35 days of ERS and Envisat satellites, to 12 hours (at 40°latitude, in case of emergency response) of the COSMO-SkyMed constellation (Casagli et al., 2017). The enhanced spatial resolution (azimuth x range) of images spans in the order of few meters (i.e. 1-10 m), resulting more detailed with respect to the resolution of the first-generation satellites characterized by pixel sizes of 10-30 meters (Plank, 2014).

Among the most advanced SAR spaceborne systems (Casagli et al., 2017), there are those of the mission Sentinel-1 operated by the European Space Agency (ESA) in the frame of the European Union’s Copernicus Programme. Satellites Sentinel-1A and 1B acquire images characterized by a spatial resolution up to 5x5 m, depending on the acquisition mode, and a temporal resolution ranging from 6 to 12 days according to the surveyed geographic area. The Sentinel-related products have a global coverage and are freely available to all users registered on the ESA data hub (<https://scihub.copernicus.eu/>). This is a



considerable benefit that is leading many research institutions and public administrations to use Sentinel data to investigate
100 landslides and other natural processes (Salvi et al., 2012; Dai et al., 2016; Twele et al., 2016; Intrieri et al., 2018). According
to Raspini et al. (2017), the future increased number of available satellites characterized by shorter revisiting times and high
spatial resolution will offer relevant information for decision support and early warning systems. Currently, significant
limitations concern the real-time and/or quasi real-time detection of rapid flow-like mass movements, rock failures, and flash
floods characterized by evolution times ranging from minutes to hours. This poses a challenge for the geo-hydrological risk
105 management based on satellite technologies.

In this article, we present a semi-automatic procedure aimed to support the detection of rapid-moving landslides by
performing the periodic survey of unstable slopes, using spaceborne radar imagery. We focus on rapid-moving landslides
since they determine evident land cover changes with respect to slow-moving failures. The main purpose of the implemented
procedure is to emphasize areas where evident land cover changes (potentially related to slope failures) occur, facilitating the
110 following possible phases of mapping and/or field survey. In other words, the procedure allows producing a map where
pixels are ranked based on the level of change observed by comparing two consecutive satellite images. Decision makers and
emergency managers can use this map to organize possible verifications and field investigations.

The procedure is implemented in a processing chain based on free data and software, and exploits radar backscattered signals
recorded within the Sentinel-1 SAR images. The values of some parameters related to the used algorithms must be provided
115 by the user. In alternative, they can be set based on the values derived from other similar areas. The processing chain was
applied, in back analysis, to an area in Papua New Guinea that in February/March 2018 was struck by a severe seismic
sequence, which triggered numerous widespread landslides.

2 Methodology

2.1 Pre-processing of SAR images

120 The implemented procedure is based on Sentinel-1 images available in Level-1 Single Look Complex (SLC) mode, with a
VV-VH polarization and Interferometric Wide acquisition mode. Level-1 SLC products are images provided in slant range
geometry, georeferenced using orbit and attitude data from the satellite. Each image pixel is represented by a complex
magnitude value and contains both amplitude and phase information (ESA, 2018). Pre-processing of the images is performed
using the Graph Processing Tool (GPT) of the Sentinel-1 Toolbox¹, and includes the following steps: (1) thermal noise
125 removal, (2) radiometric calibration, (3) Topsar de-burst, and (4) multi-looking processes.

The thermal denoising consists in the removal of dark strips with invalid data from the original data. This operation is
performed with the SNAP algorithms by subtracting the noise vectors provided by the product annotations from the power
detected image (ESA, 2017); the radiometric calibration allows computing the slant-range radar brightness coefficient (β_0)

¹ GPT is the Command Line Interface of the Open Source software SNAP Sentinel Application Platform, version 6.0 -
<http://step.esa.int/main/toolboxes/snap/>. The source code of SNAP is available at <https://github.com/senbox-org>



(El-Darymli et al., 2014) by converting digital pixel values in a radiometric calibrated backscatter; the Topsar de-burst
130 removes black-fill demarcations between the single bursts forming sub-swaths of the IW-SLC products, allowing retrieving
single images; and multi-looking is carried out to reduce the standard deviation of the noise level and to obtain
approximately square pixels of about 14 m (mean ground resolution), by applying a factor of 1:4 (azimuth:range).
Consecutive SAR images, selected to detect amplitude changes of the radar signal (i.e. change detection), are co-registered
with a DEM-assisted procedure that uses the Shuttle Radar Topography Mission (SRTM) 1 Sec digital elevation model
135 (DEM), auto-downloaded by SNAP. After the co-registration, the resulting stacked images are filtered for speckling
reduction using the adaptive Frost filter (Frost et al., 1982), with a filter size in X and Y of 5 pixels, and a damping factor
(defining the extent of smoothing) of 2.

2.2 Detection of SAR amplitude changes

To perform the change detection analysis, the Log-Ratio (LR) index is calculated as described by Mondini (2017). This
140 index measures the change in the backscattering that might be induced by land cover changes related to both natural (e.g.,
landslides, floods, snow melting) or human-induced processes (e.g., mining activities, deforestation), in a defined time
interval. For each pair of corresponding pixels belonging to consecutive pre-processed SAR images, the Log-Ratio index is
calculated as follows:

$$145 \quad LR = \ln \left(\frac{\beta_{0,i}}{\beta_{0,i-1}} \right) \quad (1)$$

where β_0 is the radiometric calibrated backscatter (i.e., SAR amplitude), and $i, i-1$ indicate two consecutive pre-processed
SAR images. For each pair of pre-processed images, a LR layer is computed, and related pixels can be characterized by
positive or negative values, depending on the backscattering changes.

When the study area (i.e. Area of Interest - AoI) corresponds to a zone smaller than the entire LR layer, a subset is extracted
150 by using the subset tool in SNAP.

2.3 Segmentation of the Log-Ratio layer

The segmentation of the LR layer is aimed to group pixels with similar LR values into unique segments. The process is
performed with the `i.segment` module in GRASS GIS 7.4 (Momsen and Metz, 2017), using the “Mean Shift” algorithm and
the adaptive bandwidth option.

155 The first step of the Mean Shift algorithm consists in the smoothing process of the LR layer. To do this, the algorithm
requires from the user the definition of the following parameters: (i) the initial bandwidth size (hr); (ii) the spatial kernel size
(hs); (iii) the threshold (th), and (iv) the maximum number of iterations. We acknowledge that the smoothing considers the
pixel p (having value LR_p) in the center of a spatial kernel of size hs and assigns to this a mean value calculated using only



the pixels that are inside the spatial kernel, with values ranging between $(LR_p - hr)$ and $(LR_p + hr)$. The unit of measurement of
160 hs is in pixel and hr is a range of LR values. In other words, the smoothing allows that each pixel value is computed
considering all pixels not farther than the spatial kernel (hs) with a difference not larger than hr . This means that pixels that
are too different from the considered pixel p are not included in the calculation of the new value.

With the adaptive option, for each pixel p , hs is fixed whereas the bandwidth size $(hr_{ad})_p$ is recalculated to account for the
variation of the pixels values (LR in this work) across the spatial kernel centered in p . The aim is to avoid the drawbacks of a
165 global bandwidth consisting in under- or over-segmentation. More in general, the adaptive bandwidth size (hr_{ad}) is calculated
using the following equation:

$$(hr_{ad}) = avgdiff \cdot \exp\left(-\frac{avgdiff^2}{2 \cdot hr^2}\right) \quad (2)$$

170 where $avgdiff$ is the average of the differences between the value of the central pixel and the values of other pixels included
in the kernel; hr_{ad} is maximum if the $avgdiff$ is equal to the user-defined hr , which is also the upper limit of the possible hr_{ad}
values (i.e. hr_{ad} is always smaller than hr). The adaptive option is particularly useful when data are characterized by high and
abrupt spatial variability (as is the case of the LR layers), and a smoothing preserving the main discontinuities is required
(Comaniciu and Meer, 2002).

175 The Mean Shift algorithm recalculates the central pixel values until a user-defined maximum number of iterations is reached,
or until the largest shift (value difference) resulting between the central pixel and the pixels inside the kernel is smaller than
a threshold (th) defined by the user. The threshold must be bigger than 0.0 and smaller than 1.0: a threshold of 0 would allow
only pixels with identical values to be considered similar and clustered together in a segment, while a threshold of 1 would
allow everything to be merged in a very large segment (Momsen and Metz, 2017). A more or less conservative threshold
180 needs to be chosen considering the spectral properties of the analyzed image. After the smoothing, pixels in the range of the
estimated local maxima (Comaniciu and Meer, 2002), which are close to each other, are clustered and included in a new map
containing the defined segments. To reduce the “salt and pepper effect”, the segments containing less than a preferred
minimum number of pixels are eliminated, by specifying the *minsize* parameter within the *i.segment* command.

To select the appropriate parameter values (i.e. tuning), a specific analysis should be carried out interactively (manually)
185 before the implemented procedure is started. In particular, variability of the segmentation outcomes to the usage of different
values for the hs , hr and th parameters must be analyzed. This analysis is event-dependent because it can be executed using
consecutive SAR images acquired before and after a well-known landslides event occurred in the past, in the area to be
surveyed or in areas which are considered similar by geomorphologists, based on the types of land cover and expected types
of landslide. The spatial kernel size hs can be heuristically chosen according to the size of the land cover changes that should
190 be detected. Keeping constant the spatial kernel size, hr and th values can be changed iteratively, evaluating the results in



terms of number and sizes of segments generated by the Mean Shift algorithm. As general rule, one can expect that large values of hr will correspond to few (but big) segments, whereas small values of hr will determine many small segments. This is due to the fact that smoothing increases when larger values of hr are used. The effect of the variation of the value of th is expected to work in the opposite direction but being much less effective on the segmentation outcomes. The first scenario (few and very large segments) is useless since it cannot be used for geo-localize the possible land cover changes. The second scenario (many and small segments) is the result of the segmentation of the random noise of the back-scattered SAR images and it is, again, useless. We assume that a possible criterion for selecting the best values of th and hr is to search for the combination of values that optimize, at the same time, the number of segments and their average size with respect to the expected land cover changes. An example of the procedure for the selection of the best values for the th and hr parameters is described in section 3.

2.4 Identification of areas potentially affected by land cover changes

After the segmentation step, a statistical analysis of the LR values included in each segment is carried out to identify segments that, with high probability, are related to significant land cover changes.

For each segment, the arithmetic mean (μ_s) of the included LR pixel values is calculated as follow:

$$\mu_s = \frac{1}{k} \left(\sum_{j=1}^k p_j \right) \quad (3)$$

where s indicates the segment, p the pixel value and k the number of pixels in the segment. We define as “average layer”, the raster layer where at each segment is associated the corresponding value of μ_s . Afterwards, in order to filter segments and extracting only those representing significant statistical changes, the μ_s values have to be compared with reference μ and average standard deviation ($\bar{\sigma}$) related to no-change conditions. These reference figures have to be calculated before the initialization of the processing chain and after the segmentation of the event-related LR image, using preceding SAR images when no heavy rainfall, landslides and earthquakes occurred, by applying the following formulas:

$$\mu = \frac{1}{m} \left(\sum_{j=1}^m p_j \right) \quad (4)$$



220

$$\sigma_s = \sqrt{\left(\frac{1}{k-1}\right) \left(\sum_{j=1}^k p_j - \mu_s\right)^2} \quad (5)$$

$$\bar{\sigma} = \frac{1}{r} \left(\sum_{z=1}^r \sigma_{sz}\right) \quad (6)$$

where m is the total number of pixels in the pre-event LR image used as reference, p is the related pixel value, and r is the total number of segments derived from the segmentation of the event-related LR image, characterized each one by a σ_s .

225 In this way, both the μ and $\bar{\sigma}$ are calculated in a kind of “warm-up stage” of the described processing chain. Generally, suitable reference figures can be calculated since the generation of three or four reference LR layers characterized by values normally distributed (i.e. Gaussian), indicating a random nature of the LR distribution that is typical of no significant land cover changes. We highlight that, in such a case, given that LR values are typically small and positive or negative, the μ value is equal or very close to zero.

230 In this way, all the segments of the “average layer” characterized by μ_s values larger than $|\mu+(2\bar{\sigma})|$ are then extracted and classified. Segments with μ_s values lower than a confidence interval of 95% ($\mu_s < |\mu+(2\bar{\sigma})|$) are instead discarded. Segments where μ_s is greater than $|\mu+(2\bar{\sigma})|$ and smaller than $|\mu+(3\bar{\sigma})|$ are reclassified to the integer value of 2. Similarly, the values 3 and 4 are used to classify segments with μ_s values included in the range $|\mu+(3\bar{\sigma})|$ to $|\mu+(4\bar{\sigma})|$, and larger than $|\mu+(4\bar{\sigma})|$, respectively. All these segments form a new raster layer representing a map of areas characterized by relevant SAR
235 amplitude changes including those affected by rapid slope movements.

In order to refine this map, all the segments with the same values (i.e., 2, 3, or 4), that are spatially contiguous and are formed by at least a user-defined minimum arbitrary size in terms of pixels (i.e. minimum detectable landslide area) are merged together, and the following statistics are then computed: 1) count of merged segments; 2) maximum number of pixels included within a single segment; and 3) average number of pixels included within a single segment.

240 The final segment map produced by the semi-automatic chain is georeferenced in the WGS84 reference system (EPSG 4326) by means of the Terrain correction tool of SNAP.

2.5 Script implementation

Besides segmentation of the event-related LR image with tuning of related parameters, and the calculation of reference μ and $\bar{\sigma}$ related to no-change conditions, all the other described procedures have been implemented in two groups of scripts that
245 can be executed automatically.

The python-based script (Fig. 1, Data ingestion) is devoted to the automatic querying and downloading of Sentinel-1 SAR images from the ESA Sentinel Data Hub. The script, based on the SentinelSat toolbox (Kersten et al., 2018), is set to query



the Sentinel Data Hub with a daily frequency even though new images may be available every 6 or 12 days, depending on the geographic area.

- 250 The group of scripts, written in GNU/Bash programming language (Fig. 1), is aimed at: (i) pre-processing the Sentinel-1 images (section 2.1), (ii) detection of the changes in SAR amplitude and production of Log-Ratio maps (section 2.2), (iii) segmentation of the LR maps (section 2.3) and, (iv) identification of areas potentially affected by land cover changes (section 2.4). This group of scripts is executed automatically when new Sentinel-1 images are available and downloaded by the python-based script.
- 255 The bash-scripts require the following settings defined by the user: 1) the path of the folder where the downloaded SAR images are stored; 2) values of the parameters required for the segmentation (see section 2.3), and (3) the spatial coordinates of the area of interest (if it is a portion of the downloaded SAR images). No further information is needed since the commands are executed in a unique automatic sequence. To survey the same area for an unlimited time period, all these settings have to be defined only for the chain initialization.

260 **3 The Papua New Guinea test site**

We selected as test site, an area located in central Papua New Guinea (Fig. 2) that was affected by a severe seismic sequence at the beginning of 2018. On 25 February, the area was hit by a main seismic event (M7.5) followed by several aftershocks, including a M6.7 earthquake on 6 March. The strong mainshock, rather superficial with a hypocentral depth at 23.4 km (USGS, 2018), caused building collapses, road damage and widespread landslides mostly along the Tagari river valley and
265 the slopes of Mount Sisa. According to the International Federation of Red Cross and Red Crescent Societies (IFRC, 2018), more than 100 people died, most of them due to landslides.

To test the implemented procedure, we have analyzed an area of about 3000 km² in the mountainous region close to the epicenters of the mainshock (AoI in Fig. 2), where preliminary information on landslides were available (Petley, 2018a,b).

- To simulate a periodic survey covering pre- and post-earthquake periods, we downloaded 36 Sentinel-1 images from the
270 Sentinel Data Hub (<https://scihub.copernicus.eu/>) acquired along the satellite track n.82 in ascending orbit with a temporal frequency of 12 days, from 12 November 2017 to 6 June 2018. The downloaded images were used to perform a total of 17 change detection analyses which resulted in likewise LR layers, with a pixel size of about 14 m. The values of the segmentation parameters were defined with an interactive manual analysis (see section 2.3) by segmenting the “pre-post M7.5 earthquake” LR layer, selecting the spatial kernel size (*hs*) of 10 pixels (see section 2.3), and setting the maximum
275 number of iterations to 200. This size of the spatial kernel was set to 10 pixels to detect significant differences of LR values during the smoothing stage of the segmentation process, taking into account the approximate expected size of the land cover changes. In the interactive (manual) analysis, we selected bandwidth sizes (*hr*, see section 2.3) ranging from 0.0005 to 0.016, and thresholds (*th*) from 0.001 to 0.016 (Fig. 3), obtaining 20 different parameter combinations. For each couple of parameters, the number of generated segments and their average size were plotted as shown in Fig. 3. Points highlight the



280 major impact of the *hr* parameter with respect to the role played by the threshold (*th*) parameter, in defining the number of
total generated segments. Below an *hr* value of 0.004 over segmentation occur, whereas for *hr* values equal or larger than
0.004, the number of generated segments tends to become small and constant. With the aim of avoiding over segmentation
while maintaining a reasonable average size of the segments (to be able to delineate also small patches of the terrain where
changes occurred), and considering a visual inspection of the segmentation results, we decided to run *i.segment* in the semi-
285 automatic processing chain using the following set of parameters values: *hs*=10, *hr*=0.004, *th*=0.008, *minsize*=2,
iterations=200 (see section 2.3).

After the segmentation of the 17 LR layers, the segments with a minimum size of 5 pixels were extracted in the area of
interest (an example in Fig. 4d), and statistics were calculated according to the confidence intervals described in the
methodology section. We decided to select only the segments with a minimum size of 5 pixels, corresponding to a minimum
290 area of 980 m² (i.e. 196 m² · 5), after a rough evaluation of the preliminary landslide-related images published on news
websites and social networks, and considering that the occurrence of smaller mass movements in the test area were not
significant at the scale of our analysis.

In Fig. 5, statistics of the selected segments are displayed for each change detection. The analysis of the histograms revealed
that two main peaks occurred for the change detections 9 and 10. Change detection 9 considers images acquired before and
295 after the M7.5 earthquake, whereas change detection 10 the images acquired on 28 February and 12 March 2018. The first
peak highlights widespread changes related also to landslides extensively documented after the M7.5 event (Petley, 2018a).
The second peak was instead unexpected and was probably due to the occurrence of further landslides triggered by the M6.7
event on 6 March 2018. In Fig. 6, segments related to these two peaks are displayed (red pixels = change detection 9; blue
pixels = change detection 10). The map shows that the two groups of segments are in general accordance with the areas (in
300 yellow) really affected by landslides, as interpreted from the optical images available on the Planet explorer application
(Planet, 2017). Small widespread segments outside the landslide areas, mostly related to stream changes and noise, also
resulted in the AoI. Similar random segments occurred in the pre- and post-event change detections, as also displayed by
statistics in Fig. 5.

3.1 Statistical evidence of landslide-like segments

305 Clear evidence of the widespread land cover changes induced by the two earthquakes, as well as the timing of their
occurrence, resulted also from a statistical analysis of the segment areas derived from each change detection. The
comparison of some representative statistics of segment's areas related to different change detections are shown in Fig. 7.
For each comparison, four types of statistics are displayed: Quantile-Quantile (Q-Q) plot, Empirical Cumulative Distribution
Function (ECDF), Density plot, Frequency plot.

310 The first column in Fig. 7 compares areas of the segments resulted from the change detections 11 and 7, which we assume
not being affected by landslides triggered by the earthquake (i.e., NO-EVENT/NO-EVENT, where the term EVENT refers
to the earthquake shocks); the second column shows the comparison between areas of the segments resulted from change



315 detections 6 and 10, with the second including seismic-triggered landslides (i.e., NO-EVENT/EVENT); the third column indicates the comparison between areas of the segments from the change detections 9 and 10, both with landslides (i.e., EVENT/EVENT).

Clear differences can be noted between the areas distribution of segments with and without landslides (change detection 6 - change detection 10) displayed in the NO-EVENT/EVENT plots. This difference is particularly highlighted in the Q-Q plot, where the gap between the blue line representing the real distributions and the theoretical similarity condition (red line) is evident.

320 Taking into account the p-values from the Kolmogorov-Smirnov tests carried out for all the 136 distribution comparisons (the combination of 17 change detections taken 2 at a time without repetition), it arises a general similarity (i.e. p-value > 0.05) among 86 of the 95 distributions that were not affected by landslides (NO-EVENT/NO-EVENT) (Fig. 8). On the other hand, among the 30 NO-EVENT/EVENT distributions, the majority (21/30) are different. The EVENT/EVENT distribution is also different (Fig. 8).

325 We have attempted to analyze the distribution of the areas of the segments derived from the change detections to verify if they follow the empirical statistical distribution of the landslides size, as described by different theoretical models (Stark and Hovius, 2001; Malamud et al., 2004; Rossi et al., 2012; Schlögel et al., 2015).

By using the tool implemented by Rossi et al. (2012) for estimating the probability distribution of landslide areas, we verified that medium and large-scale areas of segments obtained with the change detections 9 and 10 followed a landslides-
330 like behavior. In fact, the two probability distributions obtained with a Double Pareto Simplified model (Fig. 9) resulted in inverse power law decays for medium and large areas, highlighting a moderate agreement with empirical data. A rollover (inflection) in correspondence of small areas (e.g., Malamud et al., 2004) however is not present. This can be due to a consistent detection of small changes (i.e. $\sim 1000 \text{ m}^2$) ascribable to landslides and other random land cover modifications, other than some noise. In addition, it is worth remembering that segments with areas $\leq 980 \text{ m}^2$ were not considered.

335 As shown in Fig. 9, the two analyses did not pass the Kolmogorov-Smirnov test (p-value = 0). This may be explained with the fact that the input datasets (i.e. segments area) were not obtained with a proper landslide mapping activity, as described in Guzzetti et al. (2012), but with a semi-automatic procedure that is not aimed at landslide mapping operations, as clarified in the Introduction section, but at identifying land cover changes also related to landslides. Although this, results seem to be fair consistent with curves of proper landslide inventory data (Schlögel et al., 2015).

340 4 Discussion

In this article, we describe a semi-automatic processing chain aimed at identifying SAR amplitude changes that can be partially explained by the occurrence of rapid mass movements. We have selected SAR data since they have the advantage to be not affected by the cloud cover disturbance. In fact, as described by Mondini et al. (2019), the use of SAR amplitude data can mitigate the cloud coverage issue and can allow detecting landslides that, otherwise, might remain unknown or



345 unnoticed for a long time. In this way, the procedure can be exploited for a “continuous”, in terms of time, slope monitoring
activity, even if failures occur during long-lasting periods of precipitation and persistent cloud cover that do not allow to use
optical data for a rapid and detailed landslide recognition. In the selected study area, a widespread cloud cover persisted for
several weeks during and after the seismic sequence. The first cloudless optical image of the area damaged by the seismic
shaking was published by the daily monitoring service delivered by ©2019 Planet Labs Inc. (www.planet.com) on 25 March,
350 almost one month after the M7.5 mainshock that triggered numerous landslides. The high cloud persistence is quite common
in Papua New Guinea, and in fact this is included in the cloudiest regions of the world with annual cloud frequency
(proportion of days with a positive cloud flag) higher than eighty percent (Wilson and Jets, 2016; Mondini et al., 2019). As
consequence, the use of optical data in this area, and in other mountainous regions exposed to prolonged rainfall related to
monsoons, cyclones or other persistent meteorological systems results tricky.

355 The tuning of the segmentation parameters is the key element for identifying areas affected by significant land cover
changes, also induced by rapid-moving slope movements. This process can be retained event-dependent, requiring a well-
known landslide event occurred in the past in the analyzed area or in zones with similar topographic and land use
characteristics. In the case study here described, definite values of the segmentation parameters were obtained by segmenting
the pre-post M7.5 earthquake LR layer, by testing different values combinations (Fig. 3). This may represent a limit of the
360 proposed procedure if one would apply it in different geomorphic settings without past landslide events, or identifying
different types of slope failures. On the other hand, if a proper event-based tuning operation is performed, a continuous
monitoring of slopes can be efficiently carry out without temporal limitations, exploiting both pre- and post-event available
images, as done in the current case history. The described application highlighted in fact that by keeping the same
parameters values, landslides and other land cover changes triggered by the M6.7 aftershock were also detected. The
365 occurrence and location of these secondary failures (blue pixels in Fig. 6) were not known before our analysis because not
reported by news and local government websites, and also missing in the maps of the Copernicus Emergency Management
Service (<https://emergency.copernicus.eu/mapping/list-of-components/EMSR270>) activated for the disaster response. The
general lack of information related to these failures was likely due to a series of issues affecting both the field and the
satellite surveys in the aftermath of the M6.7 earthquake. In fact, an effective assessment in the field was impeded by the
370 road damages caused by the mass movements triggered by the previous major M7.5 event, whereas the use of optical
satellite images was hampered by a widespread cloud cover that, as stated before, persisted during several weeks after the
two main seismic shaking. The first information about the occurrence of these landslides were provided online by Petley
(2018b), about one month later, without a clear indication of their relationships with the M6.7 earthquake. The detection of
this second set of failures in areas poorly affected by slope movements triggered by the M7.5 event demonstrates the relevant
375 usefulness of the proposed processing chain.

The segments located outside the landslide-affected areas are caused by other land cover changes that are out of the aims of
this study, or by random noise effects. Segments related to these changes can be easily identified because composed by an



average number of pixels close to ten, as detected in all the change detections, whereas segments related to landslides (i.e. change detections 9 and 10) are characterized by a higher number pixels (Fig. 5c).

380 A suitable segmentation can allow hence to get statistical evidences of event landslides occurrence. Statistical distributions of the three parameters shown in Fig. 5 provide distinctive signatures of widespread land cover changes triggered by the M7.5 mainshock and by the M6.7 aftershock. It is worth noting, however, that 95-percentiles highlighted in the plots are exceeded also by other peaks (e.g., change detection 13 in the segment count), that cannot be considered as diagnostic of landslide occurrence since they are ephemeral, and are not steady in all the three plots as the change detections 9 and 10. In

385 case of small-scale landslides occurring in localized portions of a wide area, the related statistical signals may result imperceptible if these are of the same magnitude of other previous and successive signals not related to landslides. In cases like this, distinctive evidence of slope failures can be achieved by starting the process chain with a smaller subset of the LR layer (i.e. monitored area).

Overlapping between the segments (i.e. change detections 9 and 10) to ground truth data revealed that largest SAR amplitude

390 changes correspond often with landslides (Fig. 6). A further evidence was provided by the statistical distributions shown in Fig. 9, resulted similar to those estimated by other landslide-related studies (Stark and Hovius, 2001; Malamud et al., 2004; Rossi et al., 2012; Schlögel et al., 2015).

The outcomes of this study represent a concrete example on how to exploit the relevant advantages of Open Source software with a command line interface (i.e. SNAP and GRASS GIS) to implement automatic processing chains. Moreover, it is

395 worth noting that the proposed methodology can be properly adopted to monitor areas in the order of thousands of square kilometers if powerful hardware resources are available. In fact, the pre-processing and segmentation steps require significant amounts of calculation power and memory. It is well known that the Mean Shift is a time-consuming algorithm for large datasets (Wu and Yang, 2007), and convergence for large areas can be reached in dozens of hours. Segmentation times are proportional to the dimensions of the monitored area, and to the selected spatial kernel size (*hs*).

400 A final remark concerns the occurrence of landslides in the study area. Generally, landslides in the mountainous sectors of Papua New Guinea are very common processes. Earthquakes with a magnitude greater than 5 are among the dominant factors triggering widespread landslides. According to Robbins and Petterson (2015), such earthquakes occur regularly in the country but records of the triggered landslides are surprisingly lacking. The lack of systematic reporting and the remoteness of communities affected by such events, also impeded an adequate characterization of landslide hazard and risk (Blong,

405 1986). Robbins et al. (2013) stated that landslides occur annually, and failures tend to range from few cubic meters of material to mass movements with estimated volumes of 1.8×10^9 m³, varying from debris slides, avalanches and flows to translational and rotational slides. In this framework, the landslide detection procedure described in the article may result a relevant tool for local authorities of countries characterized by extensive remote areas repeatedly affected by slope failures, and for the humanitarian organizations operating in response to geo-hydrological disasters.



410 5 Conclusions

This study presented a semi-automatic procedure aimed to support the detection of rapid-moving landslides on vast mountainous areas. It is based on SAR data acquired systematically by the Sentinel-1 satellites. The computation of the Log-Ratio index and segmentation of the consequent raster layers allow detecting areas affected by multi-temporal variations of the radar backscattered signal. Among them, areas potentially related to rapid-moving landslides are identified with a robust
415 statistical analysis. The performance of the implemented procedure was tested in back analysis on an area of about 3000 km² in Papua New Guinea. Here, in 2018, two consecutive earthquakes (M7.5 and M6.7) triggered widespread slope failures causing more than 100 fatalities and severe damage to roads and buildings. The simulation of a multi-temporal survey of about seven months, before and after earthquakes, revealed the ability of the implemented procedure to detect statistical evidences of significant land cover changes in correspondence of the two events. Moreover, results demonstrated that the
420 zones affected by landslides were identified with a fair accuracy, as compared to the ground truth data.

The study highlighted advantages of free SAR products that may guide the scientific community and the local authorities to develop archives of freely accessible data, suitable for implementing streamlines of information aimed to monitor natural and urbanized areas. As demonstrated in the case study, the proposed procedure has the potential to be a valid support in landslide emergency management, providing in near real-time relevant information for civil protection authorities and
425 scientists involved in the emergency response. Future improvements may limit the user decisions in the model parameterization, optimizing the processing times and refining the filtering of landslide-related changes by considering also geological and geomorphological factors.

Author contributions. IM, GE and AM designed and realized the processing chain. GE and IM carried out the experiments.
430 GE wrote a first draft of the manuscript. MR and GE carried out statistics about landslide-like segments. IM, GE and PR analyzed the results. GE, SS, IM and PR improved the final manuscript version.

Competing interests. The authors declare that they have no conflict of interest.

Acknowledgements. The research was developed in the framework of the STRESS (Strategies, Tools and new data for REsilient Smart Societies) project, funded by Cariplo, focusing on designing, implementing and testing of a Spatial
435 Information Infrastructure, enabling the provision to spatial planners and risk managers of new data and tools to improve susceptibility, hazard and impact assessment of geo-hydrological phenomena.
(http://www.idpa.cnr.it/progetti_STRESS_ufficiale.html).

References

- Alvioli, M., Mondini, A. C., Fiorucci, F., Cardinali, M., and Marchesini, I.: Topography-driven satellite imagery analysis for
440 landslide mapping, *Geomat. Nat. Haz. Risk*, 9(1), 544–567, doi:10.1080/19475705.2018.1458050, 2018.
- Blong, R.J.: Natural hazards in the Papua New Guinea highlands, *Mt. Res. Dev.*, 6, 233–246, doi: 10.2307/3673393, 1986.



- Bornaetxea, T., Rossi, M., Marchesini, I., and Alvioli, M.: Effective surveyed area and its role in statistical landslide susceptibility assessments, *Nat. Hazards Earth Syst. Sci.*, 18, 2455–2469, doi:10.5194/nhess-18-2455-2018, 2018.
- 445 Calò, F., Calcaterra, D., Iodice, A., Parise, M., and Ramondini, M.: Assessing the activity of a large landslide in southern Italy by ground-monitoring and SAR interferometric techniques, *Int. J. Remote Sens.*, 33(11), 3512–3530, doi:10.1080/01431161.2011.630331, 2012.
- Calvello, M., Peduto, D. and Arena, L.: Combined use of statistical and DInSAR data analyses to define the state of activity of slow-moving landslides, *Landslides*, 14(2), 473–489, doi:10.1007/s10346-016-0722-6, 2017.
- 450 Casagli, N., Frodella, W., Morelli, S., Tofani, V., Ciampalini, A., Intrieri, E., Raspini, F., Rossi, G., Tanteri, L. and Lu, P.: Spaceborne, UAV and ground-based remote sensing techniques for landslide mapping, monitoring and early warning, *Geoenvironmental Disasters*, 4(1), 1–23, doi:10.1186/s40677-017-0073-1, 2017.
- Cigna, F., Bianchini, S., and Casagli, N.: How to assess landslide activity and intensity with persistent scatterer interferometry (PSI): the PSI-based matrix approach, *Landslides* 10(3), 267–283, doi:10.1007/s10346-012-0335-7, 2013.
- 455 Colesanti, C. and Wasowski, J.: Investigating landslides with space-borne Synthetic Aperture Radar (SAR) interferometry, *Eng. Geol.*, 88(3–4), 173–199, doi:10.1016/j.enggeo.2006.09.013, 2006.
- Comaniciu, D. and Meer, P.: Mean shift: A robust approach toward feature space analysis, *IEEE Trans. Pattern Anal. Mach. Intell.*, 24(5), 603–619, doi:10.1109/34.1000236, 2002.
- 460 Dai, K., Li, Z., Tomás, R., Liu, G., Yu, B., Wang, X., Cheng, H., Chen, J. and Stockamp, J.: Monitoring activity at the Daguangbao mega-landslide (China) using Sentinel-1 TOPS time series interferometry, *Remote Sens. Environ.*, 186, 501–513, doi:10.1016/j.rse.2016.09.009, 2016.
- El-Darymli, K., McGuire, P., Gill, E., Power, D. and Moloney, C.: Understanding the significance of radiometric calibration for synthetic aperture radar imagery, *Can. Conf. Electr. Comput. Eng.*, (May), doi:10.1109/CCECE.2014.6901104, 2014.
- 465 ESA, Thermal Denoising of Products Generated by the S-1 IPF, 2017, available at: <https://sentinels.copernicus.eu/documents/247904/2142675/Thermal-Denoising-of-Products-Generated-by-Sentinel-1-IPF> (last access: 04 January 2020).
- ESA, Level-1 SLC Products, 2018, available at: <https://sentinel.esa.int/web/sentinel/user-guides/sentinel-1-sar/product-types-processing-levels/level-1> (last access: 04 January 2020).
- Fiorucci, F., Cardinali, M., Carlà, R., Rossi, M., Mondini, A. C., Santurri, L., Ardizzone, F., and Guzzetti, F.: Seasonal landslides mapping and estimation of landslide mobilization rates using aerial and satellite images, *Geomorphology* 129 (1–2), 59–70, doi:10.1016/j.geomorph.2011.01.013, 2011.
- 470 Frost, V. S., Stiles, J. A., Shanmugan, K. S., and Holtzman, J. C.: A Model for Radar Images and Its Application to Adaptive Digital Filtering of Multiplicative Noise. *IEEE T. Pattern Anal. Mach. Intell.*, PAMI-4, 157–166, 1982.
- Gabriel, A. K., Goldstein, R. M., and Zebker, H. A.: Mapping small elevation changes over large areas: differential radar interferometry, *J. Geophys. Res.*, 94, 9183–9191, doi:10.1029/JB094iB07p09183, 1989.



- 475 Guzzetti, F., Cardinali, M., Reichenbach, P., Carrara, A.: Comparing landslide maps: a case study in the upper Tiber River Basin, Central Italy, *Environ. Manage.*, 25 (3), 247–363, doi:10.1007/s002679910, 2000.
- Guzzetti, F., Mondini, A. C., Cardinali, M., Fiorucci, F., Santangelo, M. and Chang, K. T.: Landslide inventory maps: New tools for an old problem, *Earth-Science Rev.*, 112(1–2), 42–66, doi:10.1016/j.earscirev.2012.02.001, 2012.
- International Federation of Red Cross and Red Crescent Societies (IFRC), Emergency Plan of Action Operation Final Report
- 480 - Papua New Guinea: earthquake, available at: https://reliefweb.int/sites/reliefweb.int/files/resources/MDRPG008dfr_0.pdf (last access: 24 January 2020), 2018.
- Intrieri, E., Raspini, F., Fumagalli, A., Lu, P., Del Conte, S., Farina, P., Allievi, J., Ferretti, A. and Casagli, N.: The Maoxian landslide as seen from space: detecting precursors of failure with Sentinel-1 data, *Landslides*, 15(1), 123–133, doi:10.1007/s10346-017-0915-7, 2018.
- 485 Kersten, Valgur, M., Marcel, W., Jonas, Delucchi, L., unnic, Kinyanjui, L. K., Schlump, martinber, Baier, G., Keller, G., Castro, C.: *sentinelsat/sentinelsat: v0.12.2 (Version v0.12.2)*, Zenodo, doi:10.5281/zenodo.1293758, 2018
- Konishi, T. and Suga, Y.: Landslide detection using COSMO-SkyMed images: A case study of a landslide event on Kii Peninsula, Japan, *Eur. J. Remote Sens.*, 51(1), 205–221, doi:10.1080/22797254.2017.1418185, 2018.
- Li, N., Wang, R., Deng, Y., Liu, Y., Li, B., Wang, C., and Balz, T.: Unsupervised polarimetric synthetic aperture radar
- 490 classification of large-scale landslides caused by Wenchuan earthquake in hue-saturation-intensity color space, *J. Appl. Remote Sens.*, 8, doi:10.1117/1.JRS.8.083595, 2014.
- Ma, H.R., Cheng, X., Chen, L., Zhang, H., and Xiong, H.: Automatic identification of shallow landslides based on Worldview2 remote sensing images, *J. Appl. Remote Sens.*, 10(1), 016008, doi:10.1117/1.JRS.10.016008, 2016.
- Malamud, B. D., Turcotte, D. L., Guzzetti, F., Reichenbach, P.: Landslide inventories and their statistical properties, *Earth*
- 495 *Surf. Proc. Land.*, 29(6), 687–711, doi: 10.1002/esp.1064, 2004.
- Marchesini, I., Ardizzone, F., Alvioli, M., Rossi, M., and Guzzetti, F.: Non-susceptible landslide areas in Italy and in the Mediterranean region, *Nat. Hazards Earth Syst. Sci.*, 14, 2215–2231, doi:10.5194/nhess-14-2215-2014, 2014.
- Martha, T. R., Kerle, N., Van Westen, C. J., Jetten, V. and Kumar, K. V.: Segment optimization and data-driven thresholding for knowledge-based landslide detection by object-based image analysis, *IEEE Trans. Geosci. Remote Sens.*, 49(12
- 500 PART 1), 4928–4943, doi:10.1109/TGRS.2011.2151866, 2011.
- Mergili, M., Marchesini, I., Alvioli, M., Metz, M., Schneider-Muntau, B., Rossi, M., and Guzzetti, F.: A strategy for GIS-based 3-D slope stability modelling over large areas, *Geosci. Model Dev.*, 7, 2969–2982, doi:10.5194/gmd-7-2969-2014, 2014a.
- Mergili, M., Marchesini, I., Rossi, M., Guzzetti, F., and Fellin, W.: Spatially distributed three-dimensional slope stability
- 505 modelling in a raster GIS, *Geomorphology*, 206, 178–195, doi:10.1016/j.geomorph.2013.10.008, 2014b.
- Momsen, E. and Metz, M.: *i.segment*, available at: <https://grass.osgeo.org/grass74/manuals/i.segment.html> (last access: 07 January 2020), 2017.



- Mondini, A. C.: Measures of spatial autocorrelation changes in multitemporal SAR images for event landslides detection, *Remote Sens.*, 9(6), doi:10.3390/rs9060554, 2017.
- 510 Mondini, A. C., Chang, K. T., and Yin, H. Y.: Combining multiple change detection indices for mapping landslides triggered by typhoons, *Geomorphology*, 134, 440–451, doi:10.1016/j.geomorph.2011.07.021, 2011.
- Mondini, A. C., Santangelo, M., Rocchetti, M., Rossetto, E., Manconi, A. and Monserrat, O.: Sentinel-1 SAR amplitude imagery for rapid landslide detection, *Remote Sens.*, 11(7), 1–25, doi:10.3390/rs11070760, 2019.
- Petley, D.: An emerging crisis? Valley blocking landslides in the Papua New Guinea highlands, available at:
515 <https://blogs.agu.org/landslideblog/2018/02/28/papua-new-guinea-crisis/> (last access: 24 January 2020), 2018a.
- Petley, D.: Papua New Guinea earthquake – continued landslide impacts, available at:
<https://blogs.agu.org/landslideblog/2018/03/14/papua-new-guinea-earthquake-3/> (last access: 24 January 2020), 2018b.
- Planet Team, Planet Application Program Interface: In Space for Life on Earth, San Francisco, CA, available at:
<https://api.planet.com> (last access: 24 January 2020), 2017.
- 520 Plank, S.: Rapid damage assessment by means of multi-temporal SAR - A comprehensive review and outlook to Sentinel-1, *Remote Sens.*, 6, 4870–4906, doi:10.3390/rs6064870, 2014.
- Plank, S., Twele, A. and Martinis, S.: Landslide mapping in vegetated areas using change detection based on optical and polarimetric SAR data, *Remote Sens.*, 8(4), doi:10.3390/rs8040307, 2016.
- Raspini, F., Bardi, F., Bianchini, S., Ciampalini, A., Del Ventisette, C., Farina, P., Ferrigno, F., Solari, L. and Casagli, N.:
525 The contribution of satellite SAR-derived displacement measurements in landslide risk management practices, *Nat. Hazards*, 86(1), 327–351, doi:10.1007/s11069-016-2691-4, 2017.
- Reichenbach, P., Rossi, M., Malamud, B. D., Mihir, M. and Guzzetti, F.: A review of statistically-based landslide susceptibility models, *Earth-Science Rev.*, 180(November 2017), 60–91, doi:10.1016/j.earscirev.2018.03.001, 2018.
- Robbins, J. C. and Petterson, M. G.: Landslide inventory development in a data sparse region: spatial and temporal
530 characteristics of landslides in Papua New Guinea, *Nat. Hazards Earth Syst. Sci. Discuss.*, 3(8), 4871–4917, doi:10.5194/nhessd-3-4871-2015, 2015.
- Robbins, J. C., Petterson, M. G., Mylne, K. and Espi, J. O.: Tumbi Landslide, Papua New Guinea: Rainfall induced?, *Landslides*, 10(5), 673–684, doi:10.1007/s10346-013-0422-4, 2013.
- Rossi, M., Ardizzone, F., Cardinali, M., Fiorucci, F., Marchesini, I., Mondini, A. C., Santangelo, M., Ghosh, S., Riguer, D.
535 E. L., Lahousse, T., Chang, K. T., and Guzzetti, F.: A tool for the estimation of the distribution of landslide area in R., *Geophysical Research Abstract*, 14, EGU2012–9438–1, 2012.
- Rossi, M. and Reichenbach, P.: LAND-SE: a software for statistically based landslide susceptibility zonation, version 1.0, *Geosci. Model Dev.*, 9, 3533–3543, doi:10.5194/gmd-9-3533-2016, 2016.
- Salvi, S., Stramondo, S., Funning, G.J., Ferretti, A., Sarti, F. and Mouratidis, A.: The Sentinel-1 mission for the
540 improvement of the scientific understanding and the operational monitoring of the seismic cycle, *Remote Sens. Environ.*, 120, 164–174, doi:10.1016/j.rse.2011.09.029, 2012.



- Santangelo, M., Marchesini, I., Bucci, F., Cardinali, M., Fiorucci, F., and Guzzetti, F.: An approach to reduce mapping errors in the production of landslide inventory maps, *Nat. Hazards Earth Syst. Sci.*, 15, 2111–2126, doi:10.5194/nhess-15-2111-2015, 2015.
- 545 Schlögel, R., Malet, J. P., Reichenbach, P., Remaître, A. and Doubre, C.: Analysis of a landslide multi-date inventory in a complex mountain landscape: the Ubaye valley case study, *Nat. Hazards Earth Syst. Sci.*, 15, 2369–2015, doi: 10.5194/nhess-15-2369-2015, 2015.
- Shimada, M., Watanabe, M., Kawano, N., Ohki, M., Motooka, T. And Wada, Y.: Detecting Mountainous Landslides by SAR Polarimetry: A Comparative Study Using Pi-SAR-L2 and X-band SARs, *Trans. Japan Soc. Aeronaut. Sp. Sci.*
- 550 *Aerosp. Technol. Japan*, 12(ists29), Pn_9-Pn_15, doi:10.2322/tastj.12.pn_9, 2014.
- Skriver, H.: Crop classification by multitemporal C- and L-band single- and dual-polarization and fully polarimetric SAR, *IEEE Trans. Geosci. Remote Sens.*, 50(6), 2138–2149, doi:10.1109/TGRS.2011.2172994, 2012.
- Stark, C. P. and Hovius, N.: The characterization of landslide size distributions, *Geophys. Res. Lett.*, 28, 1091–1094, doi: /10.1029/2000GL008527, 2001.
- 555 Steger, S., Brenning, A., Bell, R., Petschko, H. and Glade, T.: Exploring discrepancies between quantitative validation results and the geomorphic plausibility of statistical landslide susceptibility maps, *Geomorphology*, 262, 8–23, doi:10.1016/j.geomorph.2016.03.015, 2016.
- Tessari, G., Floris, M. and Pasquali, P.: Phase and amplitude analyses of SAR data for landslide detection and monitoring in non-urban areas located in the North-Eastern Italian pre-Alps, *Environ. Earth Sci.*, 76(2), 1–11, doi:10.1007/s12665-017-
- 560 6403-5, 2017.
- Twele, A., Cao, W., Plank, S. and Martinis, S.: Sentinel-1-based flood mapping: a fully automated processing chain, *Int. J. Remote Sens.*, 37(13), 2990–3004, doi:10.1080/01431161.2016.1192304, 2016.
- United States Geological Survey (USGS), Event page of the M 7.5 Papua New Guinea earthquake occurred on February 25, 2018, Available at: <https://earthquake.usgs.gov/earthquakes/eventpage/us2000d7q6/executive#executive> (last access: 07
- 565 January 2020), 2018.
- van Westen, C. J., van Asch, T. W. J., Soeters, R.: Landslide hazard and risk zonation — why is it still so difficult?, *B. Eng. Geol. Environ.*, 65, 167–184, doi:10.1007/s10064-005-0023-0, 2006.
- Wilson, A. M. and Jetz, W.: Remotely Sensed High-Resolution Global Cloud Dynamics for Predicting Ecosystem and Biodiversity Distributions, *PLoS Biol.*, 14(3), e1002415, doi: 10.1371/journal.pbio.1002415, 2016
- 570 Wu, K. L. and Yang, M. S.: Mean shift-based clustering, *Pattern Recognit.*, 40(11), 3035–3052, doi:10.1016/j.patcog.2007.02.006, 2007.
- Yamaguchi, Y.: Disaster Monitoring by Fully Polarimetric SAR Data Acquired With ALOS-PALSAR, *P. IEEE*, 100(10), 2851–2860, doi:10.1109/JPROC.2012.2195469, 2012.



575 Zhao, C., Lu, Z., Zhang, Q., and De La Fuente, J.: Large-area landslide detection and monitoring with ALOS/PALSAR
imagery data over Northern California and Southern Oregon, USA, *Remote Sens. Environ.*, 124, 348–359,
<https://10.1016/j.rse.2012.05.025>, 2012.

Zhao, C., Zhang, Q., Yin, Y., Lu, Z., Yang, C., Zhu, W., and Li, B.: Pre-, co-, and post- rockslide analysis with
ALOS/PALSAR imagery: A case study of the Jiweishan rockslide, China. *Natural Hazards and Earth System Sciences*
13, 2851-2861, 2013.

580

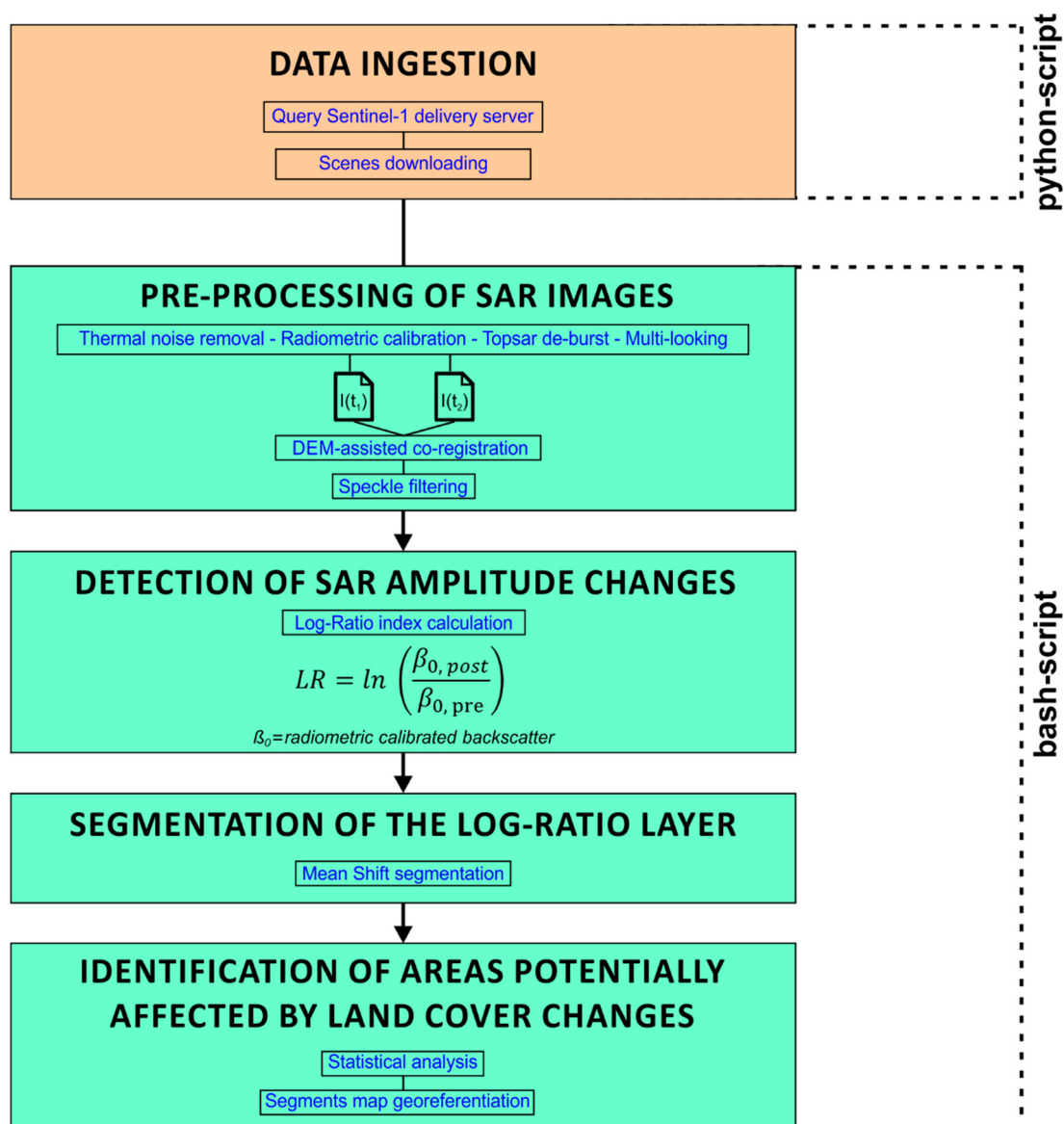


Figure 1: Flowchart of the automatic steps of the processing chain described in the text. The single steps are grouped in two main scripts (developed using Python and Bash scripting languages). $I(t_1)$ and $I(t_2)$ represent two consecutive SAR images (or set of images).

585

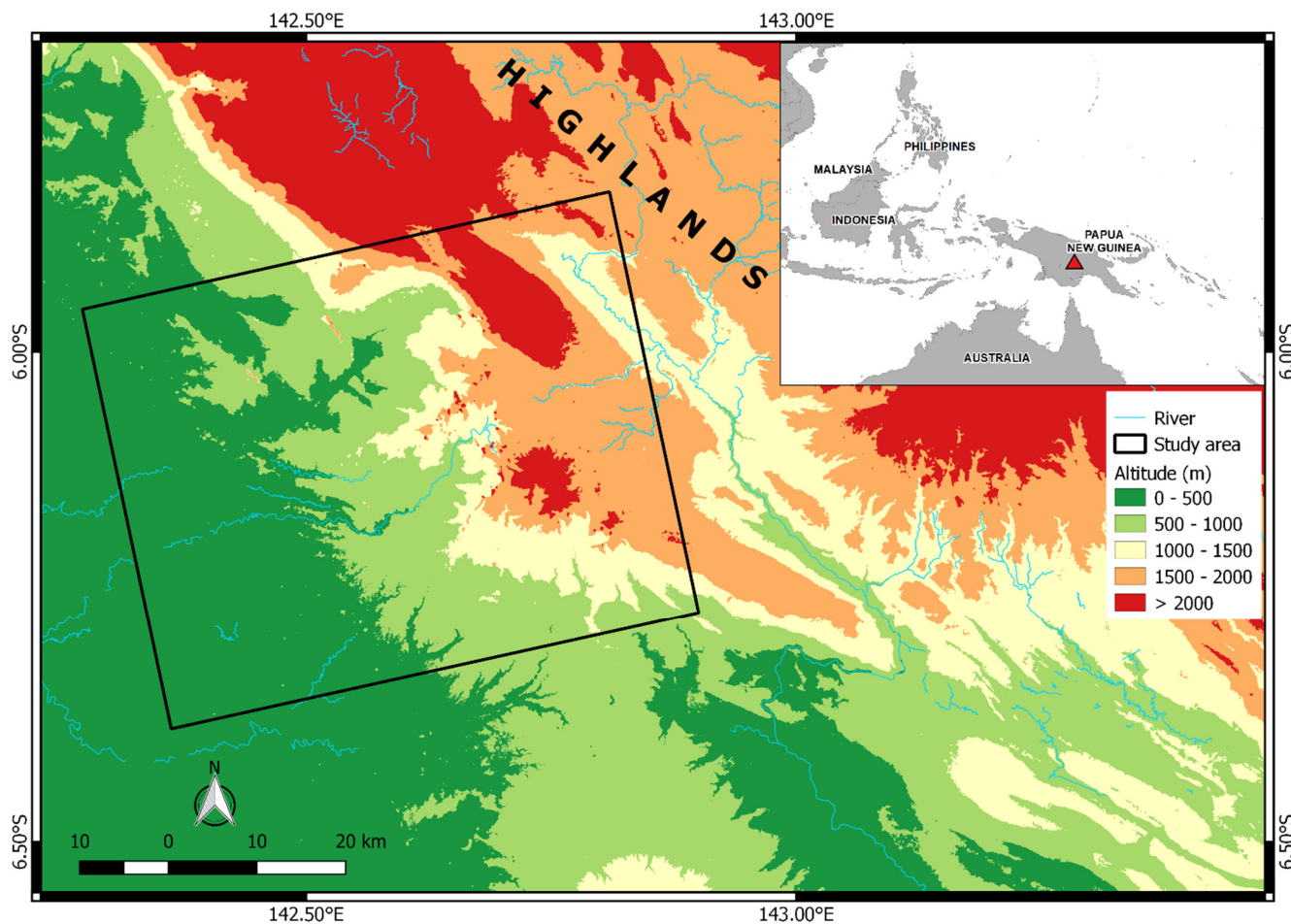


Figure 2: Location of the test site. The Area of Interest (AoI) is shown with a black rectangle in the main map and with a red triangle in the inset.

590

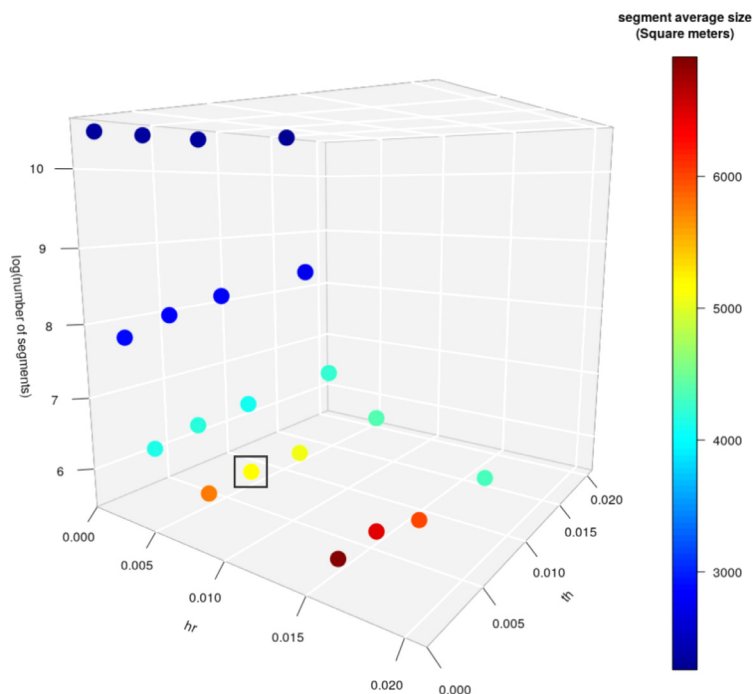
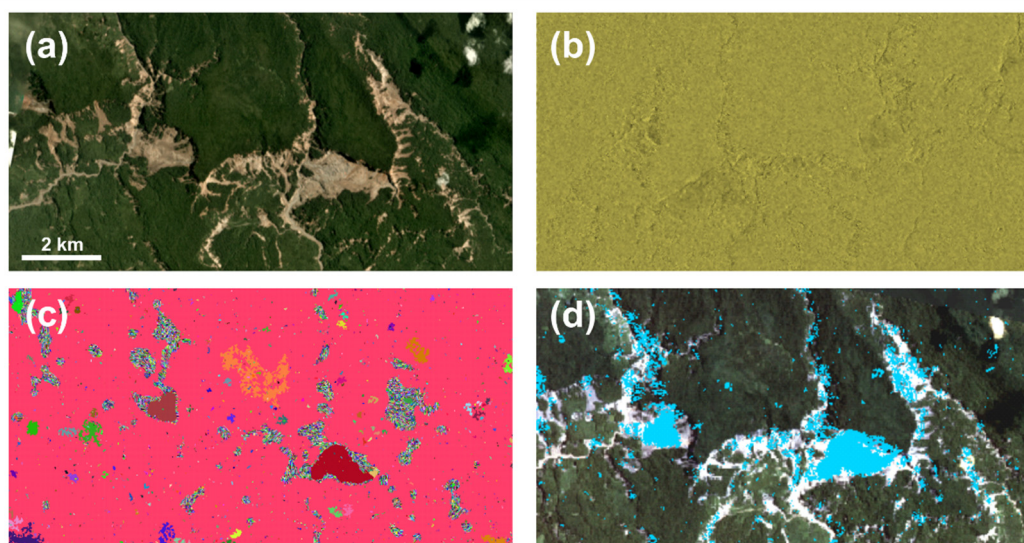
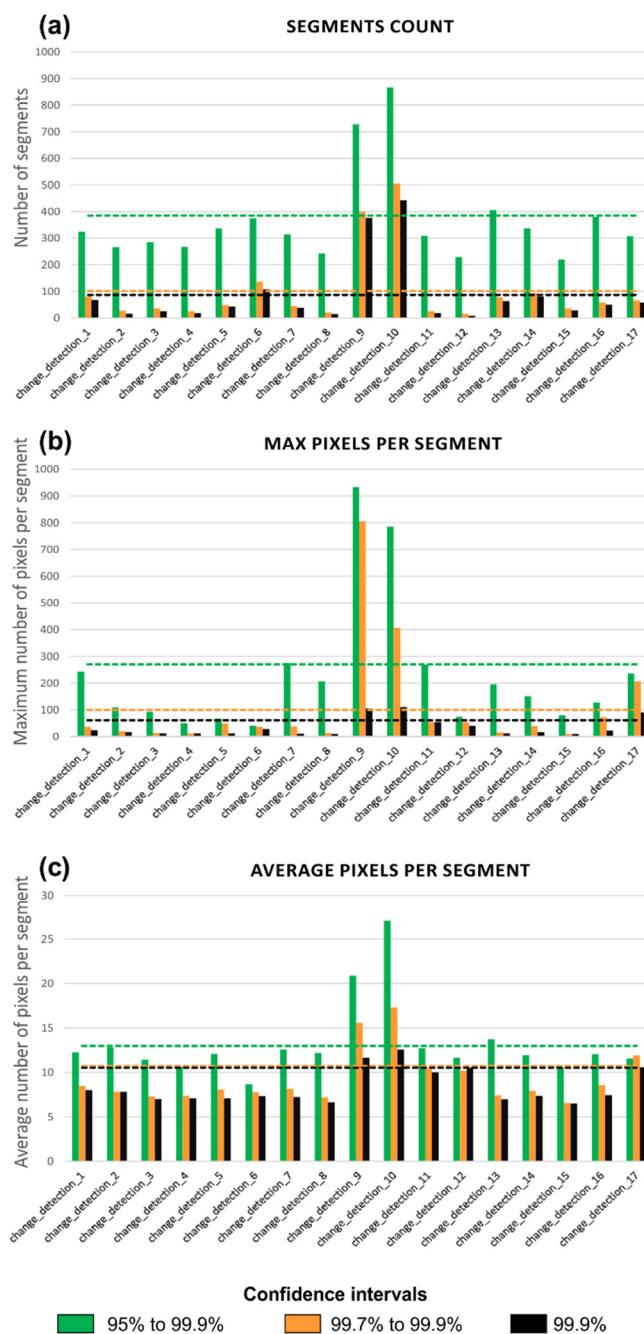


Figure 3 - Data analysis aimed at evaluating the best combination of bandwidth (hr) and threshold (th) values. The black rectangle identifies the selected combination.



595

Figure 4 - a) Optical image of a small sample area affected by landslides within the AoI; b) the corresponding Log-Ratio layer; c) the output of the segmentation algorithm (obtained using the optimized hr and th values); d) the extracted landslide-related segments (in blue).

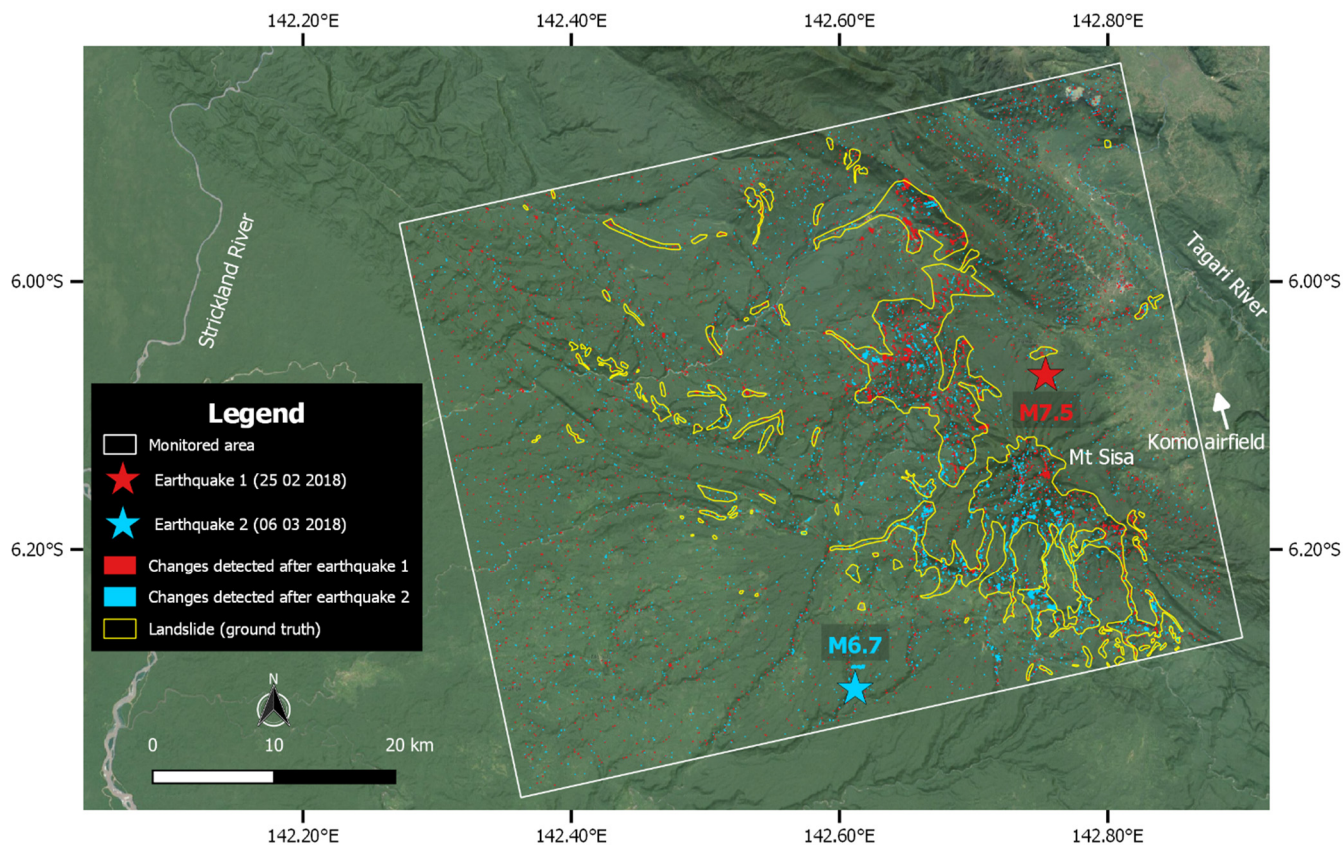


600

Figure 5 - Statistics of the segments identified for each change detection. a) number of segments with more than 5 pixels; b-c) maximum and average number of pixels per segment. For the change detections 9 and 10, the two peaks indicate the occurrence of

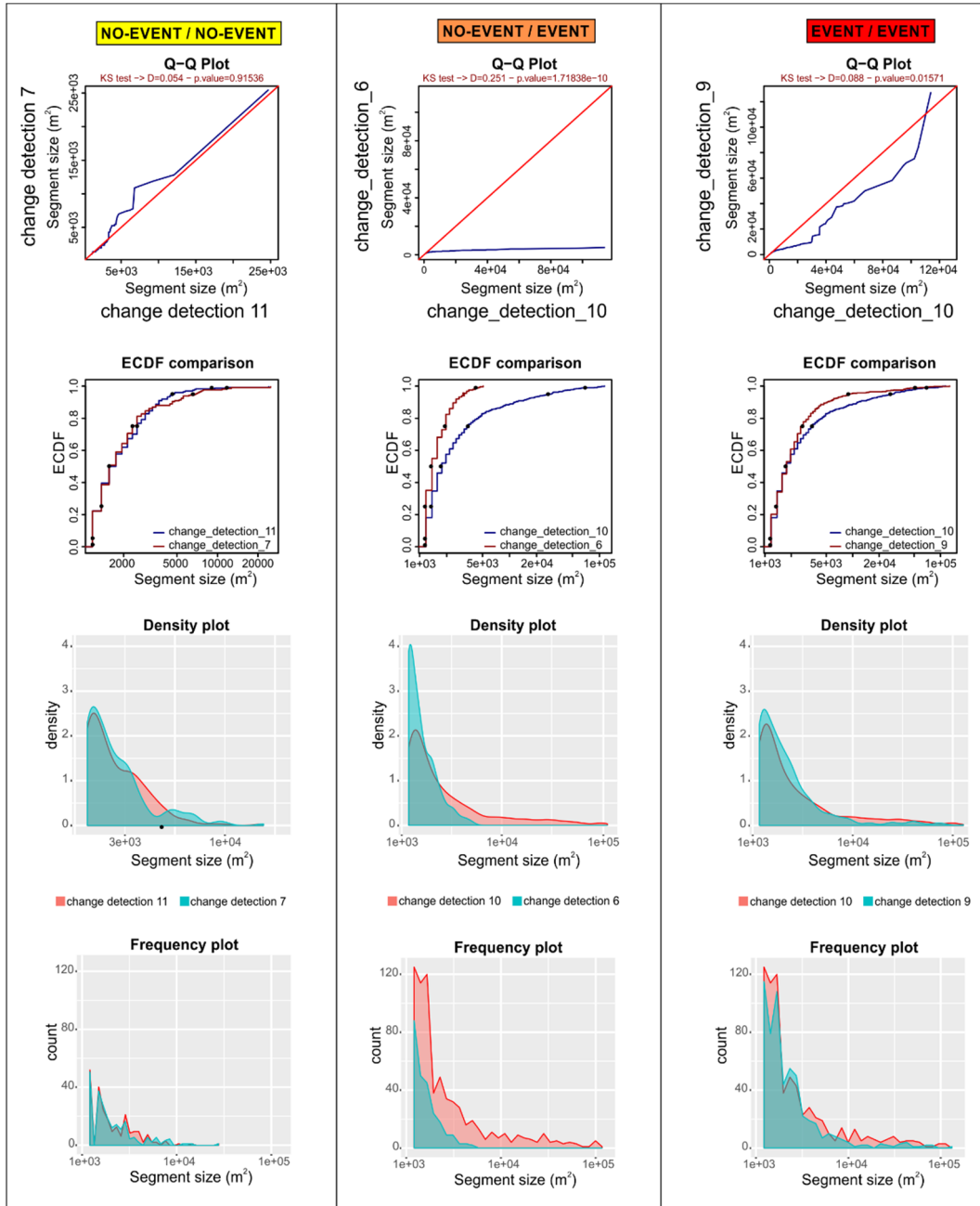


widespread land cover changes. The dashed lines show the 95° percentiles of the distributions (not including change detections 9 and 10).



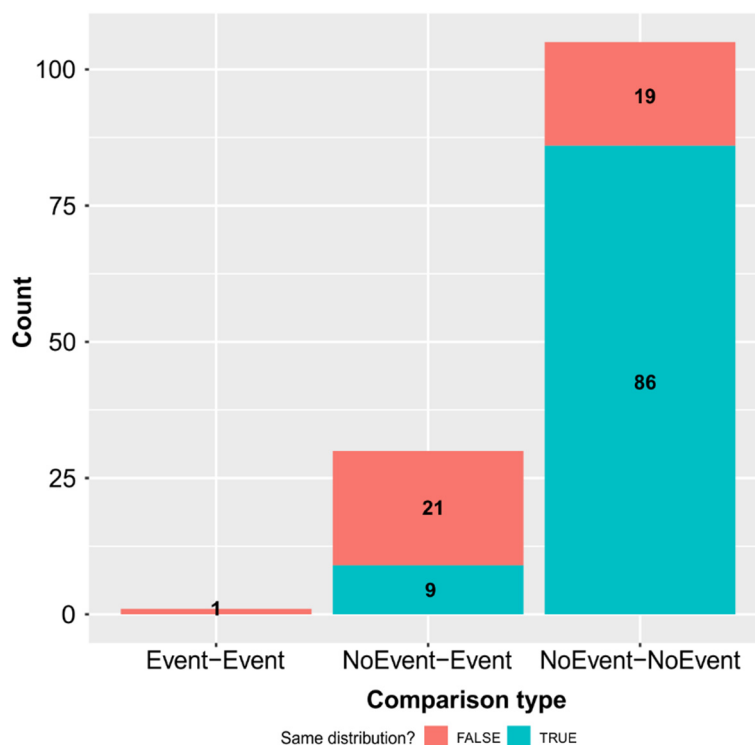
605

Figure 6 - The map shows location of the epicenters of the two main earthquakes, and the distribution of segments representing SAR amplitude changes for the change detections 9 and 10. Yellow polygons are areas really affected by landslides. The white rectangle identifies the AoI (see Figure 2).



610

Figure 7 - Comparison of segment's areas statistics related to different change detections.



615 **Figure 8 - Histogram representing the differences, calculated according to the p-value of the Kolmogorov-Smirnov tests, between all the compared distributions.**

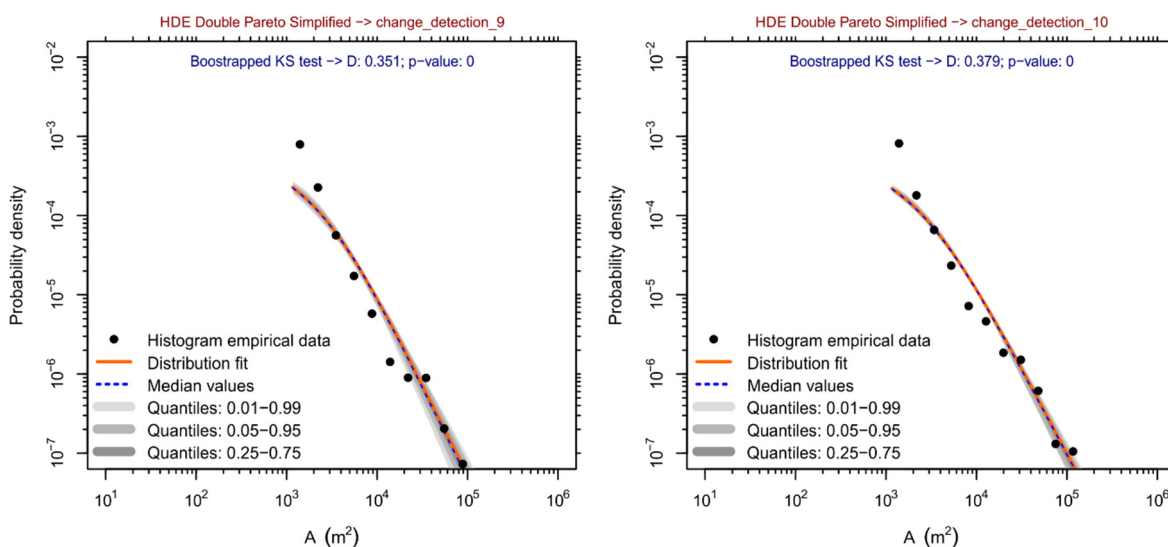


Figure 9 - Frequency - area distribution of segments resulted in the change detections 9 (on the left) and 10 (on the right), and fitting with a Double Pareto simplified model.